Ⓔ

Geophysical Evidence for a San Andreas Subparallel Transtensional Fault along the Northeastern Shore of the Salton Sea

by Valerie Sahakian,[*] Annie Kell, Alistair Harding, Neal Driscoll, and Graham Kent

Abstract The southern San Andreas fault (SSAF) accommodates a significant amount of strain between the Pacific and North American plates; thus, the fault represents a major geohazard to the populated areas of southern California, in particular the larger Los Angeles metropolitan area. Paleoseismic chronology of ruptures along the SSAF segment suggests this fault is near the end of its interseismic period (∼180 years), because it has not ruptured in historic times (∼320 years). A recent active-source seismic experiment performed in the Salton Sea west of the SSAF provides evidence for extensional deformation along the northeastern shore of the Salton Sea. This study posits that the extensional deformation is due to a previously unmapped fault, here named the Salton trough fault (STF). The seismic reflection data image a divergent sediment package that dips toward the northeast with thicknesses up to at least 2 km. Refraction inversion produces a southwestward-dipping velocity discontinuity that crops out east of the SSAF surface trace, consistent with the existence of a southwest to northeast gradient in lithology. If present, the existence of the STF has scientific and societal relevance. First, the STF appears to control the recent Salton trough architecture north of Bombay Beach. Second, from a seismological hazards perspective, the presence of this structure could alter the current understanding of stress transfer and rupture dynamics in the region, as well as community fault models and ground-motion simulations on the SSAF.

Online Material: Uninterpreted seismic-reflection profiles.

Background

The southern San Andreas fault (SSAF, Fig. 1) in southern California is an important part of the Pacific–North American plate boundary system, accommodating 21–25 mm/yr of the boundary's total 50 mm/yr of slip (Bennett *et al.*, 1996; Fay and Humphreys, 2005; Lundgren *et al.*, 2009). At its southern terminus, the SSAF steps west over to the Imperial fault (IF), creating the Salton pull-apart basin through a releasing bend in the right-lateral system (Brothers *et al.*, 2009). The basin architecture is complex, involving the interaction of many fault systems including the Extra fault zone and Brawley seismic zone (Lynch and Hudnut, 2008; Brothers *et al.*, 2009). The SSAF/IF system has the potential of generating a large-magnitude earthquake (Brothers *et al.*, 2011), which would affect highly populated areas in southern California (Olsen *et al.*, 2006). Paleoseismic data indicate that there has not been a rupture on the southern (Coachella) SSAF in the last ∼320 years (Brothers *et al.*, 2011; Philibosian *et al.*, 2011). There have been at least two events on the IF during historical

times (1940 and 1976), neither of which triggered slip on the SSAF (Hartzell and Heaton, 1983; Thomas and Rockwell, 1996). Brothers *et al.* (2011) proposed yet another potential triggering mechanism unrelated to tectonic loading. They suggested that infilling of the Salton trough to ∼13 m above sea level by the captured Colorado River could load and trigger northeast-trending normal (hinge) faults observed in the Salton Sea (Brothers *et al.*, 2009), thereby increasing the coulomb stress on the SSAF and IF. Constraining the fault structure and potential fault interactions is a critical first step toward evaluating these proposed triggering mechanisms.

The Salton trough is located in the Colorado deltaic system in southern California (Waters, 1983). Prehistoric flooding of the Colorado River into the ancient Lake Cahuilla yielded high sedimentation rates in the recent geologic past, and thus a detailed record of past and present tectonic signals (Waters, 1983). Active source seismic data provide important constraints on fault architecture by imaging the deformation of the sediments and the style of faulting within and adjacent to the Salton Sea (Fig. 1). Previous studies using earthquake locations and geodetic data (Fialko, 2006) model a steep

---

*Now at Earthquake Science Center, U.S. Geological Survey, 345 Middlefield Road, Menlo Park, California 94025.
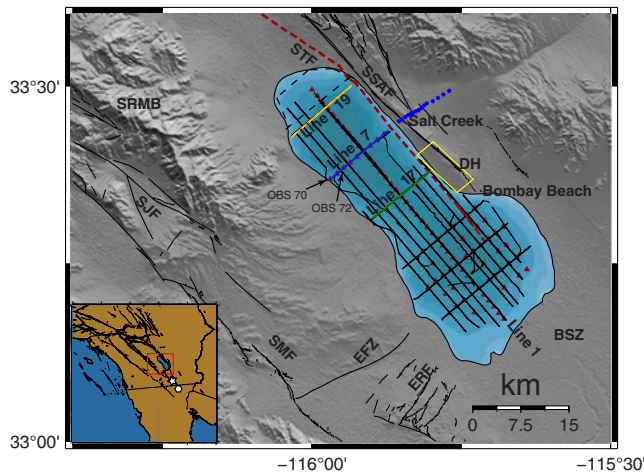
Figure 1. The inset shows the regional map of southwest United States and Mexico. The rectangle indicates the region of study. The star and hexagon represent the 1940 and 1979 Imperial fault event epicenters, respectively. The main figure shows the region of study, in which triangles denote ocean-bottom seismmeter (OBS) locations and circles denote land shots used in the velocity model for line 7. Two OBS instruments shown in Figure 4 are noted here. The box adjacent to line 17 shows the location of Figure 10. The dashed lines denote the approximate extent of the high-resolution bathymetry. Thin black lines in the sea denote all multichannel seismic (MCS) lines collected during the experiment. MCS lines 17, 7, and 19 are marked. Fine black lines are onshore U.S. Geological Survey Quaternary faults. The location of the newly identified Salton trough fault (STF) is marked (dashed where inferred and solid where direct evidence exists). SSAF, southern San Andreas fault; SJF, San Jacinto fault; SRMB, Santa Rosa Mountain block; EFZ, Extra fault zone; ERF, Elmore Ranch fault; BSZ, Brawley seismic zone; DH, Durmid Hill; SMF, Superstition Mountain fault. The color version of this figure is available only in the electronic edition.

northeastern dip on the SSAF. Imaging stratigraphy adjacent to the SAF provides direct spatial and temporal observations of fault displacement and timing, as well as the style of faulting and the local tectonic regime.

Fault systems may be imaged directly and indirectly. Direct imaging includes observation of offset strata in reflection data and fault deformation. Indirect evidence may include dipping reflectors, stratigraphic relationships, or turbidites (Kent *et al.*, 2005; Dingler *et al.*, 2009; Maloney *et al.*, 2013). Data presented in this study provide direct and indirect evidence for a fault west of the SSAF, located within the Salton Sea near the eastern shoreline, the existence of which was proposed by Babcock (1974), and Bürgmann (1991). This newly identified structure is referred to as the Salton trough fault (STF). This structure, directly imaged at one and potentially two locales, is a transtensional, right-lateral strike-slip fault with down-to-the-southwest displacement. The dip of the STF is not constrained by the new seismic data. The existence of the STF has implications for rupture scenarios in the Salton pull-apart basin, via the triggering of fault segments through dynamic and static stress loading (i.e., the SSAF, IF, and STF). Such an understanding will improve our ability to assess regional geohazards.

Methods

An active-source seismic study was conducted within the Salton Sea and acquired multichannel seismic (MCS) reflection profiling with refraction data recorded by ocean-bottom seismometers (OBS). The overarching goal was to define the displacement, dip, and timing of deformation on the SSAF, as well as the evolution of the Salton pull-apart basin (Kell, 2014). The newly acquired data provide a more comprehensive understanding of fault architecture, in addition to existing fault mappings. This survey was performed in 2010 and 2011 as two marine campaigns in conjunction with the Salton Seismic Imaging Project (SSIP, Rose *et al.*, 2013). The SSIP used land-based receivers and source locations in combination with offshore source–receiver pairs to image the overall structure within the Salton trough. The two portions of the marine campaign provided differing resolutions in the seismic profiles; 2010 employed a shallow-towed sparker source aimed to provide high-resolution images of the shallower sediment, and in 2011, a larger generator-injector (GI) gun source, towed slightly deeper, was used to resolve deeper sediments and basin structure. In 2010, MCS data were collected with a 1.6 kJ sparker source fired at ~3.125 m (1.3 s) intervals and a 24-channel streamer with 3.125 m hydrophone group spacing. A 210 cubic inch (cu. in.) or 80 cu. in. GI gun source was employed in 2011, with a target shot spacing of ~150 m (~1 min intervals) and towed at a depth of 4–5 m. A 48-channel streamer recorded these shots with 6.25 m group spacing for MCS data, towed at a depth of 4–5 m; the same 2011 GI gun shots also were recorded on OBS instruments deployed by the Scripps Institution of Oceanography OBS Lab.

This article will focus on the northern Salton Sea and will report findings from the MCS lines oriented orthogonally to the SSAF, as well as tomographic line 7. Line 7 is amphibious, as some of the SSIP land-sourced shots to the east of the SSAF were recorded on the nine OBS instruments along line 7 and were included in the tomographic inversion to constrain velocities across the SSAF (Fig. 1). The land shots used explosives weighing between 3 and 162 kg, located at an average spacing of 105 m, and buried between 2.4 and 21.9 m depth. The data gap between the last marine shot and first land shot was approximately 2 km (Fig. 2). There are no recordings of the marine shots on the land instruments.

Aerial light detection and ranging (lidar) data collected in November 2010 were used to constrain the onshore deformation (Fig. 1) and to confirm geologic mapping results from Babcock (1974). The lidar data also directed field campaigns in the region. The data were collected in a 5 km swath surrounding the Salton Sea, with vertical accuracy of approximately 9.25 cm and an average point cloud density of 5.1 points per square meter.

In 2010, swath bathymetry was collected in select regions of the northern and southern Salton Sea with a Simrad 3102 multibeam system. At a grid resolution of 1 m, these data can reveal important features on the seafloor that may
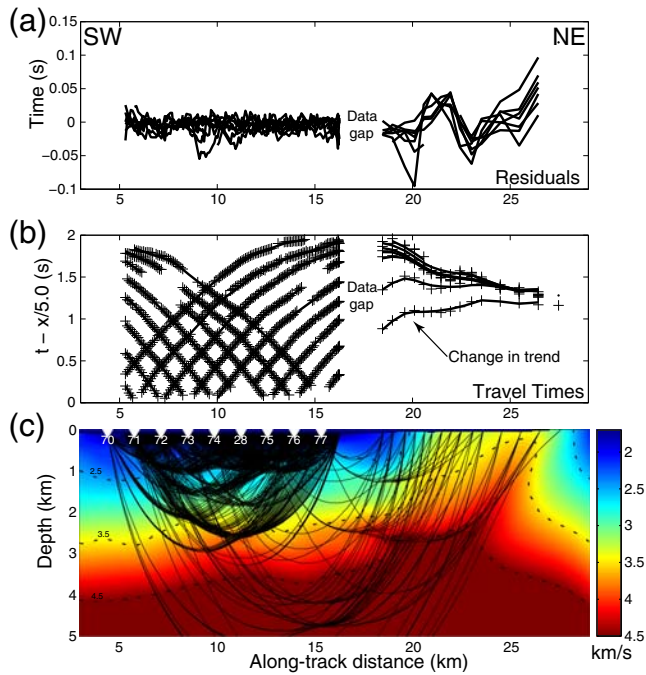
Figure 2. Initial model without the interface. The data gap between ~16 and 18 km is due to the absence of receivers or shots (both MCS and land shots) near the shoreline. This data gap is marked in (a) and (b). (a) Travel-time residuals and (b) travel-time picks plotted with a reduction velocity of 5 km/s. Hatches are the observations and the solid lines show the predicted picks. (c) Initial velocity model with ray paths plotted. OBS locations are shown by white triangles and are numbered (OBS 70–77). The color version of this figure is available only in the electronic edition.

not be resolved with MCS data. Unfortunately, due to abnormally high seawater velocity, striped along-track artifacts in the data could not be corrected.

Processing of the MCS reflection data included filtering, predictive deconvolution, and common-midpoint stacking. Travel-time picks from the OBS gathers were inverted using the method of Van Avendonk *et al.* (2004). This method iteratively reduces the travel-time residuals through a series of linearized inversions until a model with a suitable misfit (χ^2) is attained (Fig. 2). For each linearized inversion, the method minimizes a cost function that is a combination of travel-time residuals, smoothing parameters (second derivatives), and model perturbation, adjusting the trade-off between fitting and smoothing until an intermediate target misfit, compatible with linearization assumption, is obtained. The weighted misfit functional value χ^2 is given by

$$\chi^2 = \frac{1}{N} \sum_{i=1}^{N} \frac{(T_{\text{obs},i} - T_{\text{pred},i})^2}{\sigma_{\text{unc},i}}, \qquad (1)$$

in which N is the total number of picks, $T_{\text{obs},i}$ and $T_{\text{pred},i}$ are the observed and predicted pick times, respectively, and $\sigma_{\text{unc},i}$ is the assigned pick uncertainty. In this way, χ^2 is a measure of how well the model fits the data within the prescribed pick uncertainties. For the models presented here, the first arrival picks were assigned an uncertainty of 12 ms, the reflection

picks 30 ms, and second arrival picks were assigned an uncertainty of 32 ms; these picks and uncertainties are described below in further detail.

Initially, the model constructed for line 7 was generated using a 1D layered horizontal velocity model, and employed only first arrival picks from the marine and land shots recorded on the OBS instruments. The ray-path density and coverage is significantly greater offshore in the sea than it is onshore along line 7. This variation in coverage, as well as the data gap between the last marine shot and first land shot, affects the model resolution along track. The ray-path density is shown in Figure 2c, which is an example of one of the line 7 tomographic models. Here, the white triangles represent the OBS locations; the shoreline is at approximately 16.5 km along track. The data gap is noted in Figure 2a,b. The change in trend in the travel times at approximately 20 km along track is also noted. There is a notable slower trend in the near-offset arrivals (<2.5 km/s) to the southwestern edge of the profile, with faster apparent velocities (>3.5 km/s) to the northeast, indicating a lateral increase in velocity. This is likely caused by a lateral or horizontal heterogeneity in velocities, which could be represented in the model by a velocity jump.

A strong or high-amplitude reflector (HAR) is observed in the line 7 MCS stacked section (the dashed line in Fig. 3b and Ⓔ Fig. S1, available in the electronic supplement to this article). Many of the OBS shot gathers record a strong reflector, associated with a triplication in the refraction arrivals that was identified from an increase in amplitude and a rapid change in apparent velocity with offset (Fig. 4). Precritical reflections can sometimes be traced to zero offset (Fig. 4b); the vertical incidence time correlates well with the along-track arrival of the HAR in the 2011 MCS line 7 data. This evidence suggests a strong velocity contrast at depth.

Some of the models explored in this study include an interface, motivated by the complementary MCS/OBS reflections. In these models, the interface was constrained by the arrival times and dip of the HAR in the MCS stacked section (dashed line in Fig. 3b), and by picks associated with the triplication in the reflection arrivals (Fig. 4b), in which data were available. A sharp velocity contrast was imposed across the interface, as consistent with the high-amplitude MCS reflector and wide-angle reflections, as well as the change in trend observed in the OBS travel times (Fig. 2b), because it represents a change in material properties. By including this interface, these models then included first arrival picks as well as second arrival and reflection picks. These picks are assigned as either rays turning in the layer above the interface, rays turning in the layer below the interface, or rays reflecting off the interface. The onshore shots are all classified as rays turning in the layer below the interface, because of their large source-to-receiver offset. An example of the onshore shots can be seen in Figure 5. The three types of picks can be observed in Figures 4–6 (ray paths, travel times, and residuals for a model with the interface).

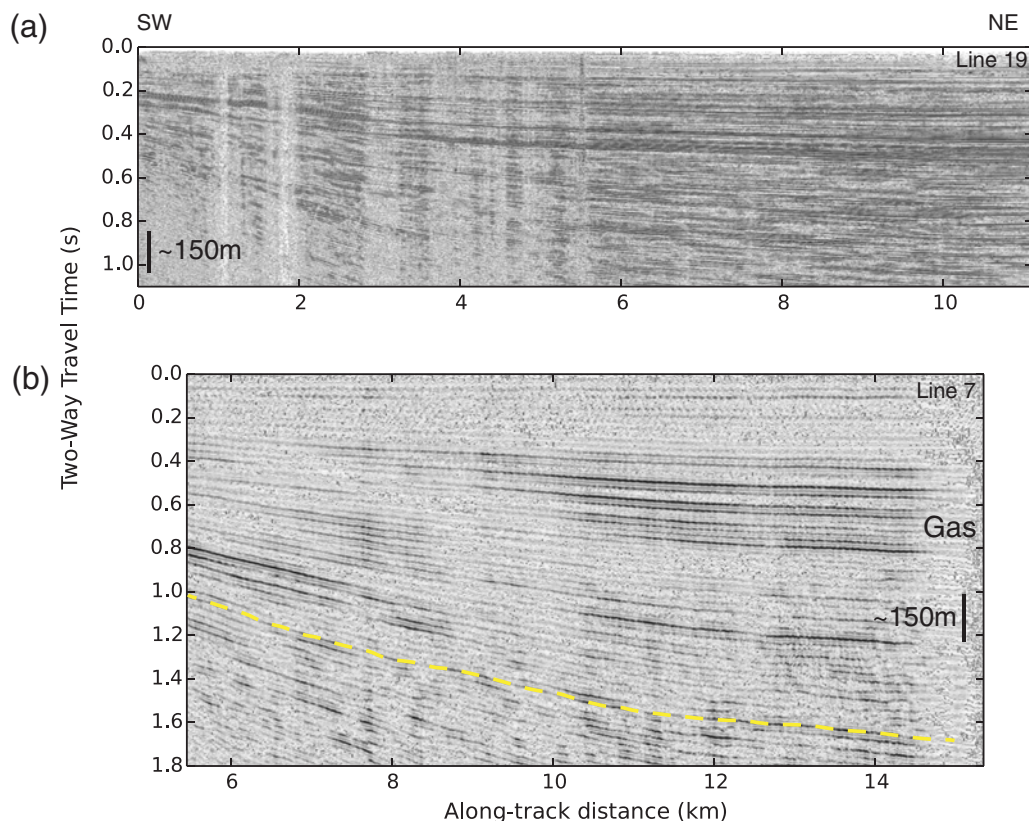The inversion simultaneously minimizes the travel-time residuals for all three picks as well as two-way travel-time

Figure 3. (a) Line 19 (2010 sparker MCS data) is the northernmost line in this study. Layers thicken and dip to the east, with no fault offset imaged within the profile. Some gas is observed in the southwest and creates vertical acoustic striping. (b) Line 7 (2011 generator-injector [GI] gun MCS data) is offshore of Salt Creek. Layers thicken and dip to the east, with the dip increasing with depth (i.e., divergent). The trend is persistent to the bottom of the profile, a depth of 1.8 s two-way travel time. The dashed line shows a high-amplitude reflector (HAR), which constrains the interface in the velocity model. Location of profiles is shown in Figure 1. The color version of this figure is available only in the electronic edition.

(TWTT) picks from the MCS reflector, and updates the model according to the new velocities of each layer as well as the depth of the interface and velocity contrast across it. For OBS 70 (Fig. 4a), both first and second arrivals turn within layer 1; the reflection cannot be discerned for this instrument, though if it were, the second arrival would be associated with its precritical reflection. OBS 72 is located at approximately 7 km along-track distance; the reflection's arrival time at this distance also corresponds to the arrival time of the HAR at ~7 km distance on MCS line 7 (Fig. 3b). The main difference between the velocity models discussed above is the location where the interface intersects the surface near the SSAF surface trace. Horizontal and vertical grid spacing for all of these models was 0.025 km. For the final model, the aspect ratio of smoothing constraints in the horizontal versus vertical direction was 5.0, and the relative strength regularization of interface depth and slowness jumps across the interface were 2.0 and 1.0, respectively.

Occasionally, the inversion stalled in local minima creating artifacts in the model that are neither required to explain the data nor are consistent with a realistic earth structure. The null space shuttles method of Deal and Nolet (1996) was employed between some inversion iterations to reduce these

artifacts. In these cases, the sedimentary section above the interface was smoothed to obtain a more homogenous velocity. This smoothed model was then projected onto the model null space. The result is a model that is consistent with the data and improves the model fit in further inversion iterations. An example of this can be observed in Figure 7. Figure 7a shows a model before applying the null space shuttles method, and Figure 7b shows the resulting smoothed model. The black ellipses indicate regions where the null space shuttles method effectively smoothed out artifacts, improving the fit to the sedimentary basin. In this example, before applying the null space shuttles method, the model's misfit stalled at $\chi^2 = 1.7$, and after applying the method and iterating further, the model's misfit improves to $\chi^2 = 1.3$.

Results

Reflection Data

This article focuses on seismic lines oriented perpendicular to the SSAF collected in the mid-to-northern Salton Sea along the western side of the SSAF (Fig. 1). Acquired with a sparker source, line 19, located ~7.5 km northwest of Salt Creek imaged layers thickening and dipping to the
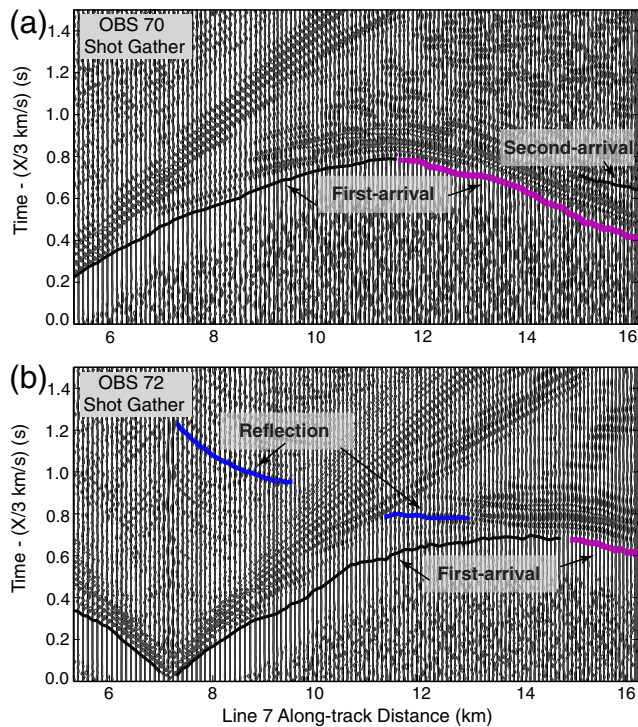
Figure 4. (a) Shot gather of OBS 70 data for shots on line 7. OBS 70 is located at approximately 4.5 km along-track distance on line 7. Picks are shown by different weighted lines (thin lines, rays that turn within the first layer; medium thickness lines, rays from reflections off the interface; thick lines, rays that turn within the second layer, below the interface). Both first and second arrivals are observed in OBS 70. (b) Shot gather of OBS 72 data for shots on line 7. OBS 72 is located at approximately 7.1 km along-track distance. Travel-time picks are shown with lines as labeled in (a). Medium thickness lines are reflections associated with the triplication. Both shot gathers are plotted with a reduction velocity of 3 km/s (see Fig. 1 for OBS locations). The color version of this figure is available only in the electronic edition.

northeast (Fig. 3a). These layers diverge with increasing dip with depth; this stratigraphic trend is persistent down to approximately 1.0 s TWTT. No fault-related offset structures are observed along line 19. To the south, line 7 (Fig. 3b) is located approximately adjacent to Salt Creek and images a similar architecture as observed on line 19 (Fig. 3a); the stratigraphic layers thicken and dip to the northeast. Line 7 was acquired with a 210 cu. in. GI gun in 2011 that yielded deeper penetration because of the lower frequency and larger sound source. This profile shows a divergent trend to at least 1.8 s TWTT (~2 km). In summary, the numerous HARs observed on lines 19 and 7 are divergent (i.e., dip increases with depth) along the northeast region of the Salton Sea with no observed offset or faulting along the profiles (Fig. 3).

Continuing farther south, line 17 (Fig. 8 and Ⓔ Fig. S2) crosses the Salton Sea slightly northwest of Durmid Hill (Fig. 1). Along both margins of the sea, the stratigraphy is obscured by gas. Within the central segment, stratigraphy is imaged down to depths greater than 1 s TWTT (~1 km). Unlike the profiles to the north (e.g., lines 7 and 19), line
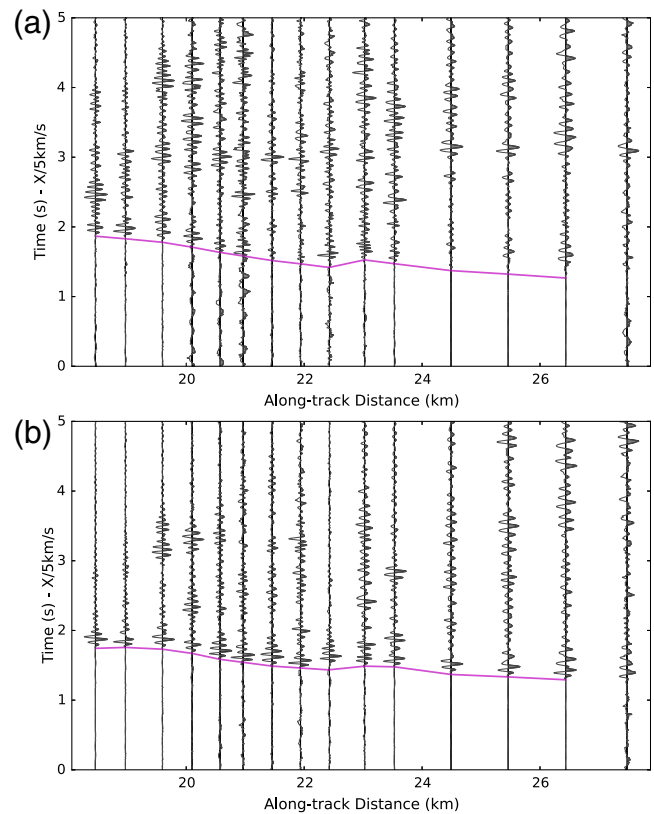

Figure 5. Onshore shots, shown here for two OBS: OBS (a) 72 and (b) 74. The shots are plotted against along-track distance with a reduction velocity of 5 km/s. The travel-time picks, all turning in the layer below the interface, are shown here as well as by a thick line. The color version of this figure is available only in the electronic edition.

17 images a fault structure at approximately 6.5 km along track, northeast of the crossing with line 1 (Fig. 1) that separates predominantly flat-lying stratigraphy to the northeast from dipping horizons to the southwest (Fig. 7 and Ⓔ Fig. S2). West of the fault, the dip of the reflectors increases downsection, from more flat-lying reflectors at the surface to an apparent 2° northeastward dip at approximately 200 m depth. Continuous undisturbed reflectors mantle the offset horizons across the fault with thicknesses on the order of 100 m. Another potential fault is observed at ~4.25 km along track, but it is obscured by gas. Toward the northeast at ~10 km along track, line 17 crosses the interpreted STF. The surficial stratigraphy east of the fault has a slight southwest dip toward the structure, with apparent dips increasing from 0° at the surface to 2° southwest at ~100 m depth. In this region, much of the stratigraphic architecture is obscured by gas, increasing uncertainty and lowering our confidence of identifying fault offsets. The presence of gas also is consistent with the existence of a fault as it would be a potential permeability pathway for fluids. Farther south, on line 16 (Sahakian, 2015), strata perpendicular to the SSAF strike are marked by diminished extension and are interrupted by transpressional faulting toward the northeast (Kell *et al.*, 2012).
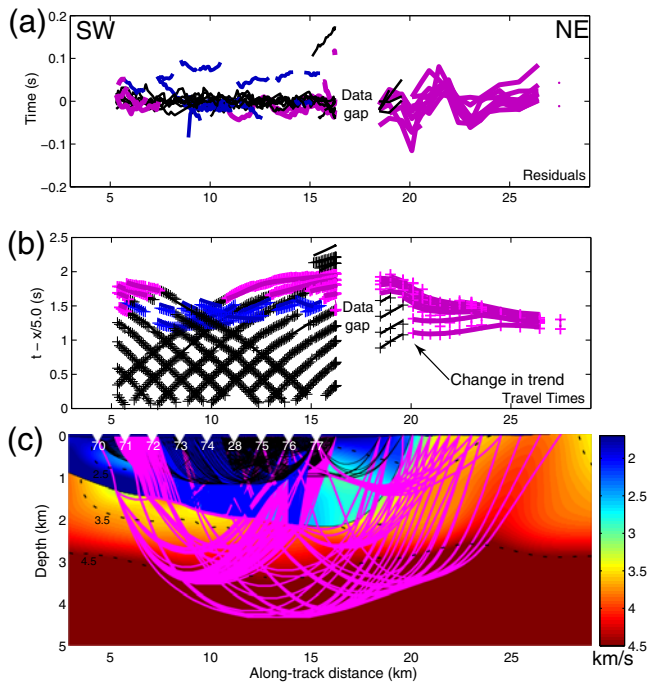
Figure 6. Preferred model E. (a) Travel-time residuals. Thick lines, rays turning within the second layer below the interface; medium lines, rays turning within the first layer, above the interface; thin lines, reflections off the interface. (b) Travel-time picks plotted with a reduction velocity of 5 km/s. Hatches are observed picks; solid lines (following the thickness scheme of panel a) are the predicted picks for the final velocity model. (c) Ray paths for the final model. The line descriptions are the same as in panels (a) and (b). White triangles denote OBS and are labeled. The color version of this figure is available only in the electronic edition.

Refraction Data

The initial homogenous velocity model and subsequent models are shown in Figure 9. Figure 9a shows topography along line 7 from the Shuttle Radar Topography Mission sampled at 1 arcsec (SRTM1; Farr *et al.*, 2007) and bathymetric data. Figure 9b–g shows the various velocity models for line 7, plotted with a mask extending 1 km horizontally and vertically beyond the ray coverage. The initial velocity model for line 7 (Fig. 9b) shows a relatively uniform velocity structure in the sea, but with an apparent southwestward dip to the velocities onshore, with an increase in velocity to the northeast. Approximately 1 km northeast of the SSAF surface trace, there is a southwestward-dipping high-velocity trend with surface expression. Along the surface, the velocity systematically increases toward the northeast for a distance of ~7 km. Velocities range from approximately 2 km/s in the shallow lake sediments to approximately 4.5–5 km/s at about 4 km depth. The final misfit is $\chi^2 = 1.4$ is low, but the model is only fitting first arrivals and includes few *a priori* constraints. At approximately 19–20 km along track (Fig. 6), a transition between two slopes or trends in the travel-time picks is not well resolved in the initial model.

Travel-time residuals, travel-time picks, and the line 7 velocity model overlain with ray paths show data coverage
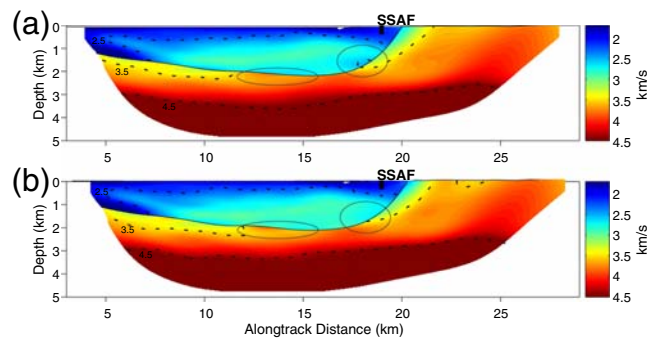

Figure 7. A velocity model for line 7. (a) Before applying the null space shuttles method and (b) after applying the null space shuttles method. Black circles in (a) and (b) denote artifacts within the lake sediments that were reduced using this method. Note the low-velocity zone above the interface is smoothed (i.e., 2.5 km/s). The color version of this figure is available only in the electronic edition.

(Fig. 2a–2c, respectively). At ~19–20 km along track, travel time trends transition from lower-to-higher apparent velocities (Fig. 2). There is a clear slower trend in the near-offset travel times (< 2.5 km/s) to the southwestern edge of the profile, with faster apparent velocities (> 3.5 km/s) to the northeast indicating a lateral increase in velocity near, but just west of the SSAF at shallow depths. Additionally, the OBS gathers record a distinct high-amplitude triplication suggesting a stronger velocity gradient than captured by the initial model (Fig. 9b). The vertical incidence time of the associated precritical reflection for each OBS matches an along-track arrival of the HAR observed in the 2011 MCS data (Fig. 3b). Later arrivals slope downward to the northeast, suggesting that high-velocity material (rocks with velocities > 4 km/s) must shallow rapidly, as observed in the initial model (Fig. 9b). These arrivals are poorly fit with the single-layer model, because smoothing does not allow juxtaposition of the fast and slow velocities laterally.

Subsequent velocity models included a defined interface in an attempt to parameterize this gradient. Models test whether a northeastward-dipping interface, as observed in the MCS data (Fig. 3b, dashed line), is consistent with the OBS data. When the refraction line overlapped with the existing MCS data, the initial depth of the interface was determined by converting the TWTT of the HAR to depth using the velocity model (Fig. 9b). Toward the northeast where MCS data were not collected, the location of the interface in the starting model was guided by the 3.2 km/s velocity contour up to the surface at a particular along-track distance. Three types of picks were assigned to constrain the model (described above in the Methods section), as well as TWTT picks from the MCS data for the reflector. This investigation resulted in seven velocity models with varying locations for the intersection of the interface with the surface (black line in Fig. 9c–g). The velocity models and their respective misfits are plotted with a mask extending 1 km beyond the ray coverage. Figure 9c–g shows the location of the interface systematically moving toward the northeast. For example, the interface in Figure 9c is 1 km southwest of the
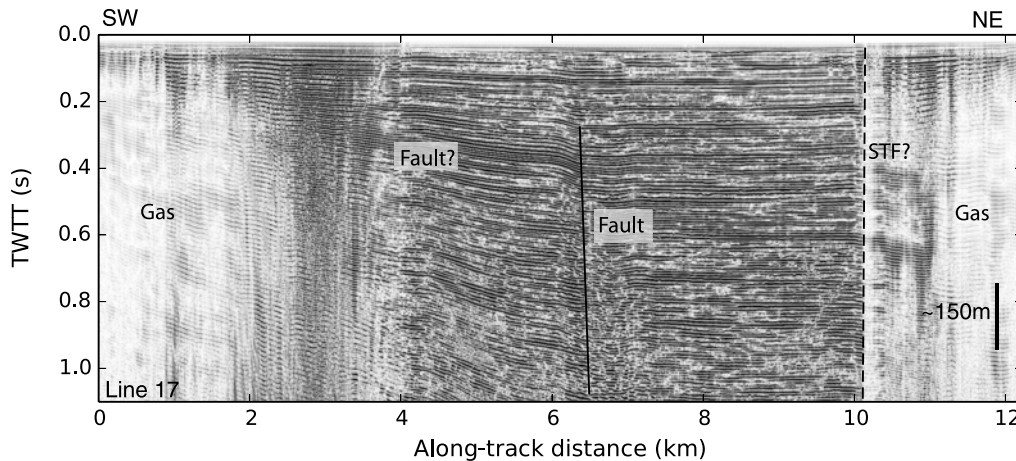
Figure 8. The 2010 sparker MCS data line 17 is located offshore just northwest of Durmid Hill. Layers exhibit slight thickening and dip to the northeast. Fault marks deformation in strata from an inactive fault. Gas is present on the southwestern and northeastern edges of the line. To the northeast, surficial reflectors appear to dip and thicken to the southwest toward a potential fault structure (STF). Location is shown in Figure 1.

SSAF surface trace and Figure 9g is 5 km toward the northeast of the SSAF surface trace. In the model shown in Figure 9d, the interface intersects the surface of the SSAF. From here on, these models will be referred to as models C, D, E, F, and G to be consistent with their figure titles. All models show similar basement velocities below the interface to the southwest of the SSAF surface trace (∼4.5 km/s). The main difference is in basin velocities near the SSAF surface trace. The most pronounced velocity differences being observed in the northeastern portion of the model.

Models C through G feature slower velocities (<3 km/s) in the basin that are similar to the sedimentary velocities in the initial starting model. The northeastern edge of the model contains higher velocities even in the shallow structures that have a western dip (Fig. 9). In models C and D, the region around the SSAF surface trace and northeast of the interface surface expression contains lower velocities in the 1.7–3 km/s range, lower than the approximately 4 km/s observed in the high-velocity region. Models C and D have misfits of $\chi^2 = 2.16$ and 1.89, respectively.

Models E, F, and G contain an interface that intersects the surface at 1, 3, and 5 km northeast of the SSAF surface trace, respectively. These models do display some medium velocity features within the basin east of the SSAF surface trace. The zones are interpreted as artifacts; the null space shuttles method had difficulty in completely smoothing the basin velocities. This feature is necessary to explain the data insofar as that some of the 3.5 km/s apparent velocity arrivals have been moved into layer 1 (basin), and the model is attempting to fit these (Fig. 6). It is important to note fewer ray-paths constrain the velocity in this region. The most interesting feature of these models is the high-velocity package to the northeast of the SSAF. All models converge to lower velocities in the region surrounding the SSAF surface trace and progressively higher velocities moving northeast (Fig. 9). They all demonstrate the possibility for a low-velocity zone adjacent to the

SSAF, skewed to the southwest. The respective misfits of models E, F, and G are $\chi^2 = 1.88$, 2.07, and 1.90.

A model with the interface intersecting the surface at 3 km to the southwest of the SSAF is not shown in Figure 9. The model with an interface at 3 km to the southwest forced the interface to have a very steeply dipping face; this created problems in convergence after only a few model iterations and as such has been omitted.

Model E is the preferred or final model, because it simultaneously fits the two trends observed in the travel-time picks while converging to the lowest misfit with an interface. Although we chose model E, model D is very similar in appearance and misfit, and could also have been selected as the preferred model. Constraints and ray paths for the final velocity model are shown in Figure 6. Figure 6a shows the travel-time picks for first and second arrivals as well as interface reflection arrivals. Ray paths are weight coded and the same for all panels. Travel-time residuals for all picks are plotted along track, as well as the final velocity model with ray paths and OBS positions (Fig. 6a,c). Note that the ray coverage is denser within the Salton Sea than onshore to the northeast (Fig. 6).

All models exhibit southwestward-dipping higher velocities on the eastern edge of the profile down to almost 3 km depth (Fig. 9). The preferred velocity model contains a dipping interface. In the southwestern portion of the profile, the interface and shallow basin velocities predominantly dip to the northeast, whereas in the eastern part of the model, they dip steeply to the southwest. All models also exhibit a low-velocity zone near the base of the sediments in the sea on the western edge (due to the absence of ray paths to update the initial velocity model here), as well as a small patch at approximately 14 km along track. It appears the low-velocity zone is due to the interplay between fast second arrivals, the location of the interface, and the smoothing constraints that influence the velocity contrast allowed across the interface.
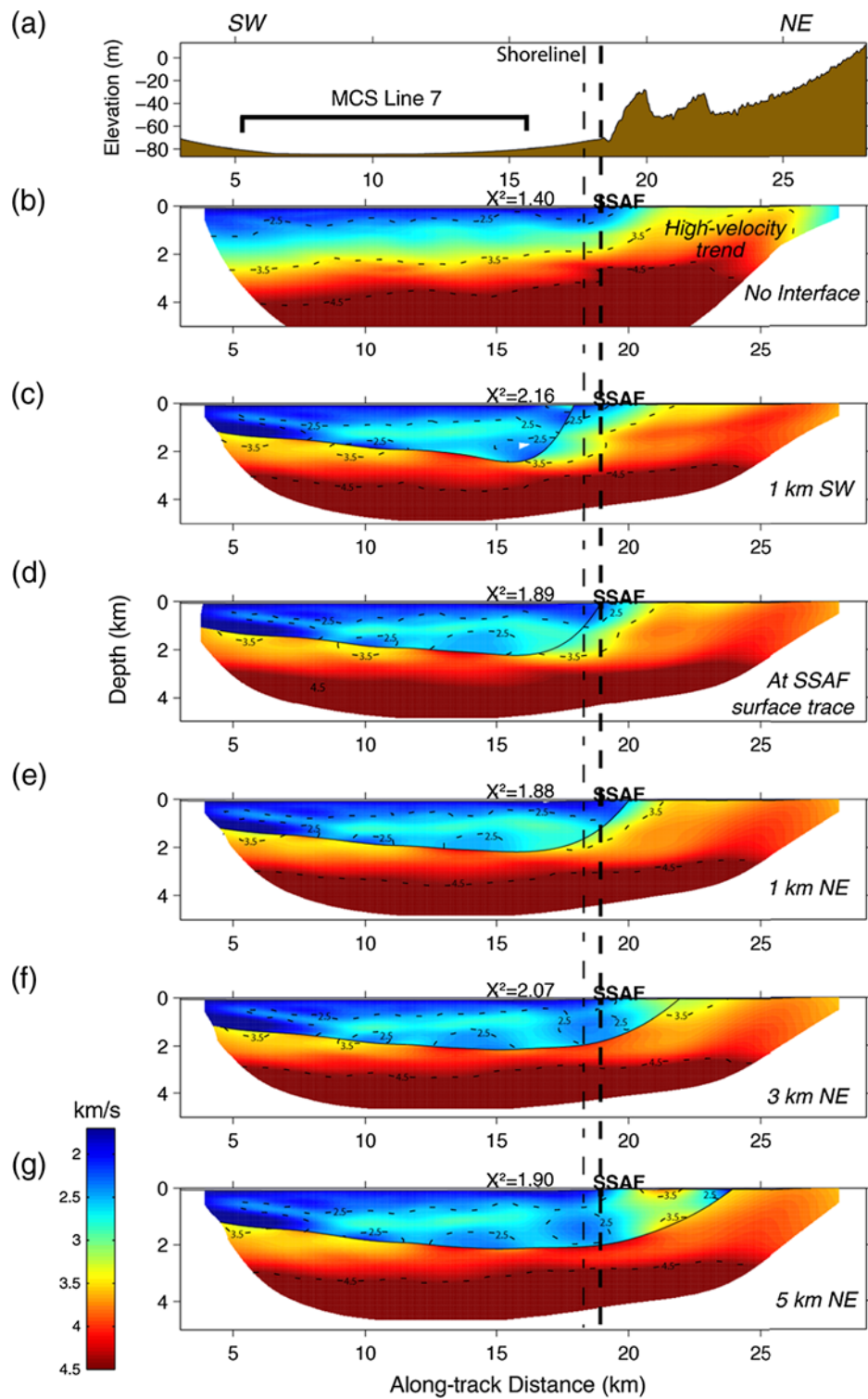
Figure 9. (a) Topographic profile of line 7 from Shuttle Radar Topography Mission sampled at 1 arcsec (SRTM1) and bathymetry data. The bar shows the location of MCS line 7; land shot locations may be observed in Figures 1 and 6. (b)–(g) Velocity models with interface. SSAF, surface trace of the SSAF. The thick dashed line shows the location of the SSAF on all the lines as well as on topography, and the fine dashed line shows the shoreline. The surface expression of the interface with respect to the SSAF is labeled on the bottom right of each panel. The misfit for each model is labeled top center. Velocity legend for all models is on the bottom left. All models are marked with a 1 km extension beyond the ray coverage. (b) Initial line 7 velocity model without interface. The shallowing high-velocity trend is labeled and is present in roughly the same region in the other models. (c) Model C with interface; the black line shows the location of the reflection interface, surfacing 1 km southwest of the SSAF surface trace. (d) Model D, with interface intersecting at the SSAF surface trace. (e) Model E, interface intersecting at 1 km northeast of the SSAF surface trace. (f) Model F, interface intersecting at 3 km northeast of the SSAF surface trace. (g) Model G, interface surfacing at 5 km northeast of the SSAF surface trace. See Figures 1 and 6 for position of land shots and OBS locations. The color version of this figure is available only in the electronic edition.
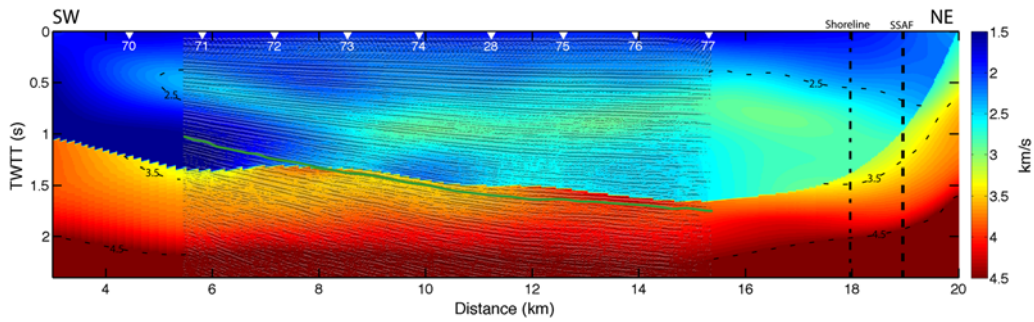
Figure 10. MCS 2011 line 7 superposed on the final velocity model after depth to time conversion. The dipping line traced on the reflection data denotes the HAR used to initially constrain the interface in the velocity model. White triangles show the OBS locations. The thick dashed line denotes the location of the SSAF, and the thin dashed line denotes the shoreline location. Velocity legend is on the right. The color version of this figure is available only in the electronic edition.
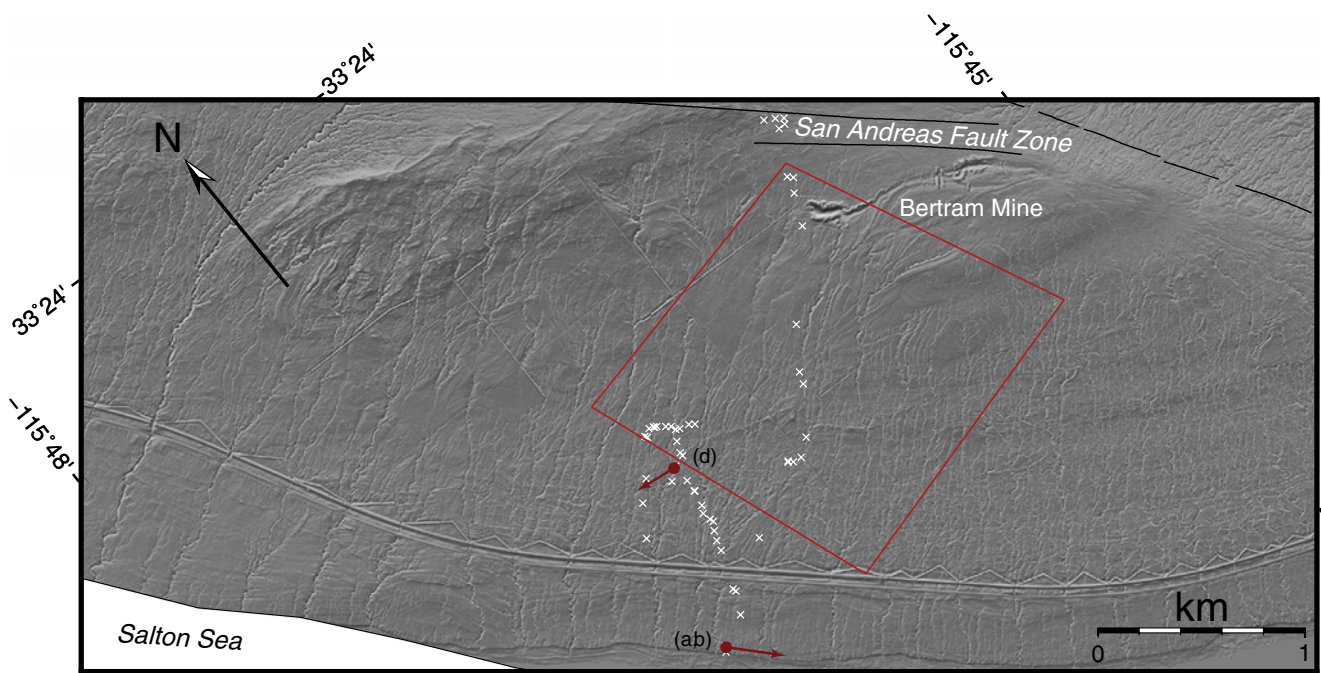

Figure 11. Aerial light detection and ranging (lidar) data from the Durmid Hill Region, with the location shown by the box in Figure 1. Here, the data are plotted at a rotated angle. White crosses show the location of field observations. The circle and arrows show the location and approximate look direction of the photographs in (a), (b), and (d). The box indicates the approximate location of (c). The curvilinear feature in the top region of the figure is Bertram mine. The SSAF zone and Salton Sea are labeled. Note the tight folding with the fold axis oriented northeast–southwest, an orientation perpendicular to the SSAF and Salton Sea shoreline. The tightness of folding changes markedly approaching the Salton Sea shoreline. The color version of this figure is available only in the electronic edition.

Figure 10 shows an overlay of MCS 2011 line 7 data with the final refraction velocity model. The solid line marks the HAR highlighted in Figure 3b. The location of the interface is not fixed, rather it varies as a function of a trade-off parameter between interface location and velocity smoothness in the layers. It is important to note that although the interface in the velocity model has been allowed to move in the inversion to fit all picks in the data, its depth is still within a maximum discrepancy of approximately 0.2 s of the HAR in the MCS data. Complete agreement between the interface and the depth of the HAR is not expected, because the

interface is parameterizing a rapid increase in velocity rather than a true geologic contact within the sea.

Geomorphic Observations

Onshore geologic observations provide additional constraints on the regional tectonics. The aerial lidar (Fig. 11) imagery shows intense folding, shortening, and truncation of folds closer to the SSAF in the Durmid Hill region (approximately onshore of line 17, Fig. 1). The strike and dip of the beds are highly variable. Both right and left-lateral offsets are
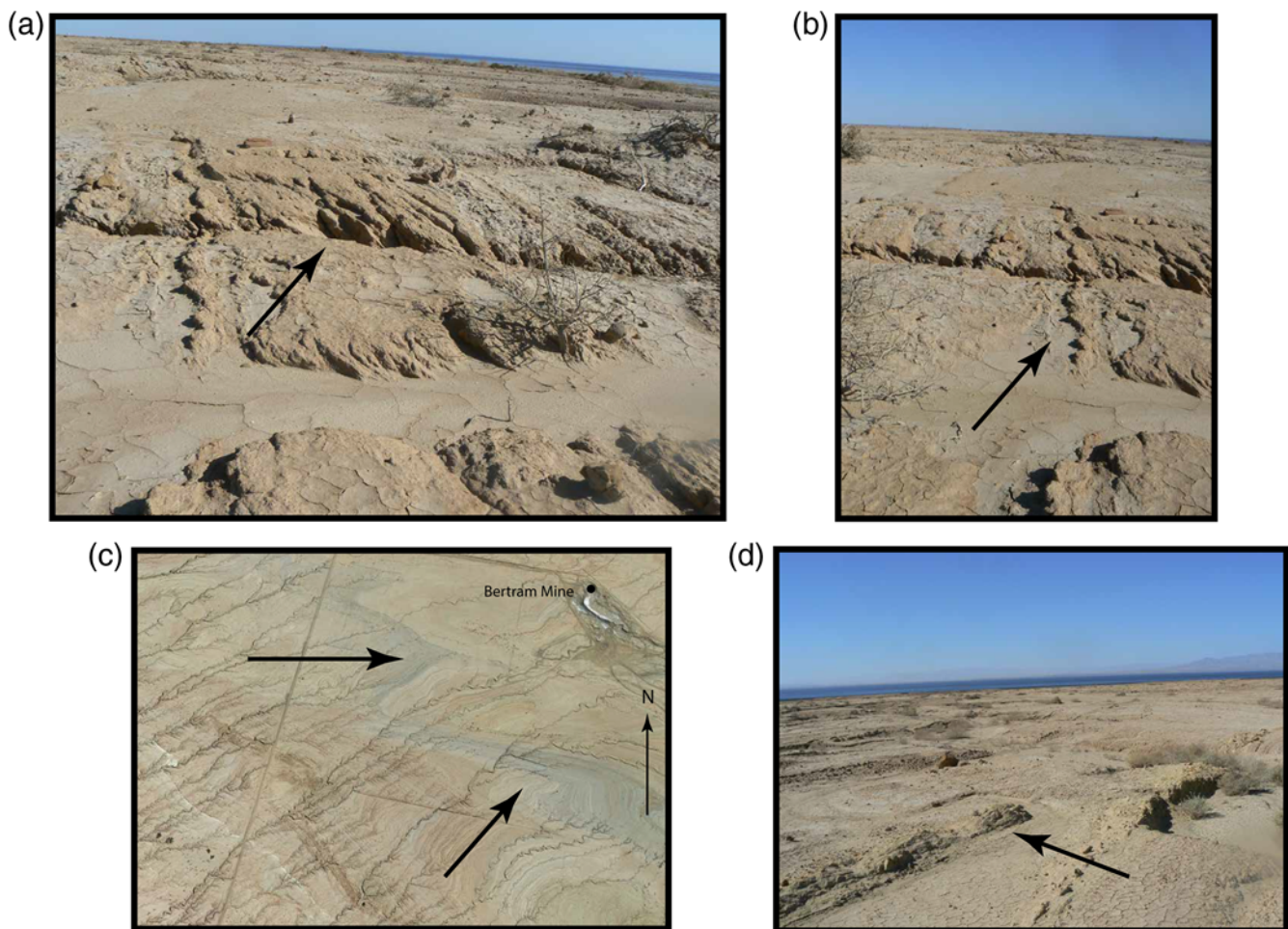
Figure 12.   The location and variable look directions of the photos in (a), (b), and (d) are shown by the circle and arrows in Figure 11. Arrows on all panels indicate the described beds and folds. (a) Beds dip to the southwest, toward the Salton Sea shoreline observed in the top right of the photo. (b) The folding is much gentler near the sea, with folds having a long wavelength. (c) Google Earth imagery showing the folds and increase in deformation near the SSAF. (d) Beds begin to transition to a longer wavelength of folding and dip to the southwest; again the Salton Sea is observed along the top of the photo. The color version of this figure is available only in the electronic edition.

observed. Moving southwest of the SSAF zone toward the Salton Sea shoreline, the wavelength of the folding becomes longer and more gentle, and the beds exhibit a much more consistent strike being subparallel to the shoreline. The dip decreases slightly toward the shoreline. White hatches denote positions of field measurements and photographs, and the circle and arrow represent the location and approximate look direction of the photos in Figure 12. The beds shown in Figure 12a and 12b have a strike and dip of N66°W and 57°SW, respectively. The onshore strata adjacent to the shoreline have a consistent southwestward dip.

The northern Salton Sea swath bathymetry data image a linear feature with a steep gradient north of and northeast of line 19; however, the bathymetric data set does not intersect with the MCS data (Fig. 3a). The strike of this feature is approximately 234°. The gradient of the data was computed in a direction perpendicular to the strike of the linear feature (the perpendicular azimuth being 144°), to improve the illumination of this feature. The bathymetric gradient and the bathymetry are shown in Figure 13a and 13b, respectively.

Figure 13c shows the values for these grids along a profile A–A′, perpendicular to the linear feature. The feature appears to be approximately 0.8 m in height.

Discussion

It is assumed that the reflector (Fig. 3b) observed in the MCS data and shot gathers has a high amplitude because of a marked impedance contrast (i.e., a physical change in stratigraphic velocity and density). The reflector TWTT observed in the seismic-reflection profile (Fig. 3b, dashed line) correlates with the zero offset arrival of the precritical reflection on each OBS instrument (Fig. 4). The character of this reflector suggests that it is not the sediment basement interface but could be related to a difference between surficial lake sediments and more indurated and compacted sediments beneath. It also could be a metamorphic contact due to emplacement of volcanic sills at depth, with thermal alteration and metamorphism of the overlying sedimentary layers (Kell, 2014).
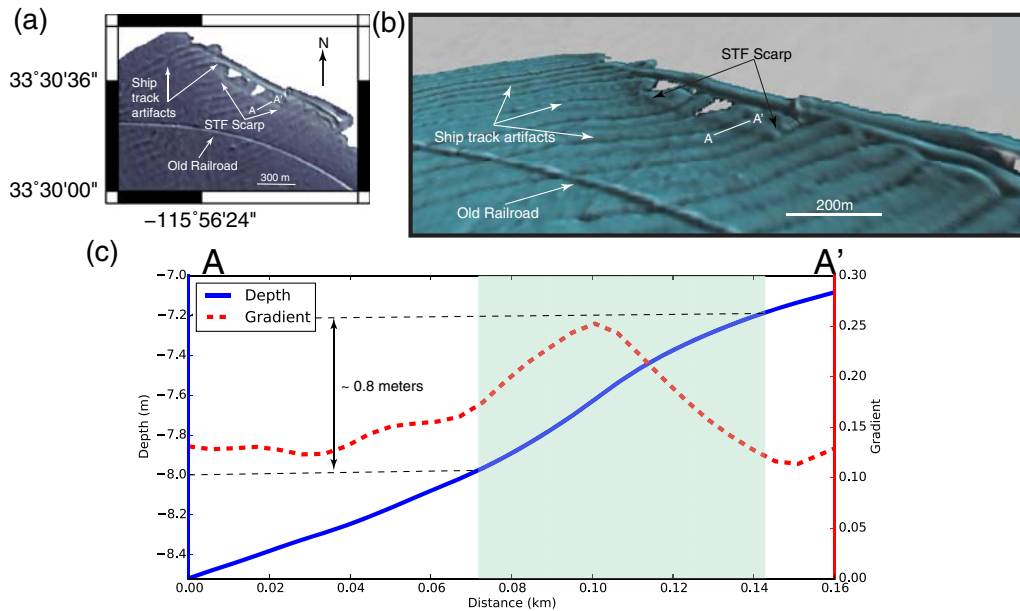
Figure 13. Northern Salton Sea swath bathymetry data. (a) The gradient of the bathymetry data, computed in a direction perpendicular to the azimuth of the notable scarp feature. The linear feature observed is on the northeastern extent of the data. The striped artifacts are still visible, as is the old submerged railroad. (b) The bathymetry, with 20× vertical exaggeration. Here, the scarp feature is denoted, as well as the ship track artifacts and old railroad. (c) A profile of the depth and depth gradient along A–A′, marked in (a) and (b). The solid line shows the depth, and dashed line shows the gradient. The thin dashed lines mark the vertical edges of the linear feature, and the shaded region marks the horizontal extent. The feature is approximately 0.8 m in height. The color version of this figure is available only in the electronic edition.

The eastward dip and thickening of layers observed in both of the MCS profiles, lines 7 and 19, suggests a dip-slip component along a vertical to slightly westward-dipping fault (Fig. 3). Motion on the hanging wall along such a fault would create increased accommodation toward the fault and a northeast dip of the reflectors. Dipping reflectors with divergence increasing down section along normal faults is diagnostic of extensional deformation, as observed in other extensional environments (Driscoll *et al.* 1995; Driscoll and Karner, 1998; Eisses *et al.*, 2015). The divergence of the layers indicates syn-depositional deformation (e.g., Fig. 3 and Ⓔ Fig. S1). The sections of gas near the eastern edge of MCS lines 7 (Fig. 3b and Ⓔ Fig. S1) and 17 (Fig. 8 and Ⓔ Fig. S2) could be evidence for a fault (STF) acting as a permeability pathway along which fluids could migrate. The potential southwestward-dipping, divergent surficial layers on the northeastern end of line 17 could be caused by extension on a fault splay in the sea. Such observations are consistent with a fault structure between approximately 10 km along-track distance (line 17) and the shoreline of the Salton Sea (Fig. 8 and Ⓔ Fig. S2).

The linear feature imaged in the bathymetric data appears to be a fault scarp. The feature does not continue farther south, but this could possibly be due to the input of sediment from Salt Creek, which would mantle the scarp and mask it in other regions. It is also possible that if this is the STF scarp, the STF may not exhibit surface expression along its entire length. Gas observed in the reflection data could be associated with fluid flow along the fault interface; however, it is difficult to discern if this is observed in the bathymetry data due to the ship track artifacts. Some evidence exists offshore

for a fault structure coincident with lines 19 and 17, but there is no offshore evidence for this fault elsewhere. There is no onshore evidence for a fault between Salt Creek (adjacent to line 7) and Durmid Hill (adjacent to and south of line 17) to explain the increased accommodation along the northeastern side of the Salton Sea. Observations of extension offshore suggest that a transtensional fault with down to the southwest displacement exists within the sea.

Babcock (1974) performed a geologic field study of the Durmid Hill area (Fig. 1), adjacent to the Salton Sea. Although there are no observations near line 7 or Salt Creek due to the fact that Lake Cahuilla sediments bury any deformation and folding, folded beds are observed several kilometers to the south, closer to line 17. Cross-sectional profiles show intense folding due to deformation associated with the SSAF zone, and all profiles show a consistent southwestward dip approaching the shoreline (fig. 8 in Babcock, 1974). The Borrego Formation, a Pleistocene brackish water lacustrine deposit, is exposed throughout most of the region of the cross sections, and younger Lake Cahuilla sands are exposed to the northwest of this area.

The aerial lidar data collected in November 2010 (Fig. 11), along with field observations and measurements of strike and dip collected during March 2015 (Fig. 12), confirm the Babcock (1974) observations of folding. It appears that the SSAF controls the intensity of folding close to the fault zone. Approaching the shoreline, the folds display a longer wavelength and demonstrate a steep (∼60°) southwestward dip toward the shoreline. The left-lateral offsets and tighter folds observed closer to the SSAF might be suggestive of
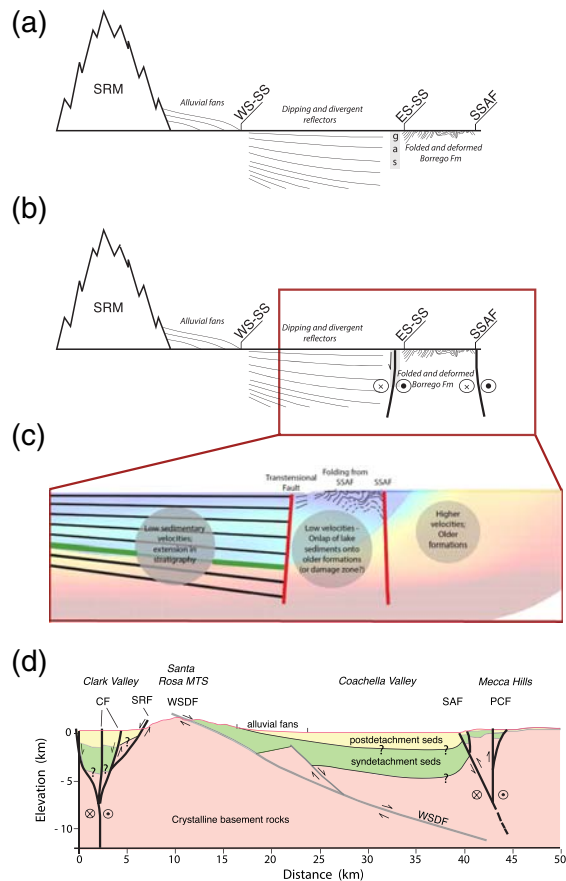
Figure 14. Schematic showing preferred hypothesis for northern Salton Sea structure. SRM, Santa Rosa Mountain block; WS-SS, western shoreline of the Salton Sea; ES-SS, eastern shoreline of the Salton Sea; SSAF, southern San Andreas fault. (a) A diagram of the structural and stratigraphic observations near line 7. Southwest of line 7 is the Santa Rosa Mountain block and alluvial fans adjacent to it, up to the western shore of the Salton Sea. Reflectors in the sea dip and are divergent toward the northeast. Gas is present just west of the shoreline. East of the shoreline, the layers in the exposed Borrego Formation dip to the southwest and are intensely folded closer to the SSAF. (b) Diagram showing the preferred hypothesis, with dipping reflectors caused by a fault to the west of the SSAF. Cross denotes away and dot denotes toward. The box delineates the area of (c). A slightly southwestward-dipping transtensional strike-slip fault is interpreted to exist near the region of gas observed in the MCS lines. The SSAF is to the northeast of the folded Borrego Formation and dips slightly to the northeast. (c) Schematic showing the observations from MCS and refraction data. The thick line in the strata on the left edge shows the HAR used to constrain the velocity model interface. The zone between the STF and SSAF is damaged and marked by a lower seismic velocity. Velocities increase to the northeast of the SSAF, with an overall southwest dip. (d) Schematic modified from Dorsey and Langenheim, 2015, showing their conceptual model explaining the rotation of the Salton Block. Question marks denote their proposed existence of formation boundaries, based on modeling efforts and not confirmed by seismic data. Extensional unloading in the southwest along the Santa Rosa fault (SRF) and compressional loading across the southern San Andreas fault (SAF) in their model engenders block rotation and the dipping reflectors observed in the postdetachment sediment wedge. WSDF, West Salton Detachment fault; PCF, Painted Canyon fault; CF, Clark fault. The color version of this figure is available only in the electronic edition.

bookshelf faulting due to deformation between these two right-lateral strike-slip faults (SSAF and STF) and their splays. Nevertheless, the folding diminishes toward the southwest, suggesting a decrease in deformation away from the SSAF.

The images in Figure 12 demonstrate the character of the beds in this location and the southwestward dip toward the sea. Examination of these features in map view makes it easy to observe the continuous spatial nature of the features. Images and data points collected in washes allow for a cross-sectional view of the beds and folding. These shoreline beds near the eastern shore of the Salton Sea show a steep southwestward dip.

No clear evidence exists in the geologic data, to date, for a significant fault onshore; however, the hypothesis of an offshore dextral fault is not new. Bürgmann (1991) mapped and modeled folding by Durmid Hill and proposed the existence of a fault offshore Durmid Hill to explain the observed characteristics. Burgmann noted that the presence of a shear zone boundary southwest of Durmid Hill could explain the folds trending subparallel with the SSAF and the tightness in folding adjacent to the SSAF. Southwest of the shoreline and for the majority of the MCS lines, layers dip and thicken toward the northeast, with apparent dips ranging from 0° to less than 2°. On line 17, some surficial reflectors on the northeastern end of the line dip to the southwest, with dips ranging from 0° to approximately 2° SW. This observation suggests the existence of a structure within the Salton Sea to focus the deformation. The collapse of these layers suggests that the structure may be transtensional in nature because the layers on both side of the fault dip toward it (fig. 4 in Eisses et al., 2015). The sediments onshore by Durmid Hill are of the Pleistocene Borrego Formation; the sediments in the sea are Lake Cahuilla sediments, much younger. It is presumed that these sediments onlap either the fault or the deformed Borrego formation very near the shoreline.

Refraction data from line 7 support this hypothesis. These data indicate that the low-velocity sediment carapace observed in the Salton Sea terminates to the east of the model boundary against the older Borrego Fmn or the inferred/interpreted structure. These very young lake sediments cannot onlap the SSAF, because these young lacustrine sediments are not observed onshore. The interface placed in the velocity model (Fig. 9) represents a velocity or density contrast. *A priori* information exists for the western end of the profile but is lacking in the eastern end. As such, the interface location in the eastern edge of the profile is more representative of a gentle gradient in velocity as opposed to a sharp contrast or jump. This is evident in the results of the models, observed in Figure 9. Regardless of location, the data require a low-velocity zone west of the SSAF (in the data gap) to be lower than velocities to the east. Similarly, the data generally require (with the exception of model C) the velocities in this region to be similar or slightly lower than the velocities observed within the sea. Northeast of this low velocity zone, the velocities increase laterally, and the zone of higher velocities extends to the surface with a southwest dip. The low-velocity zone straddles the

region around the SSAF as well as the region where a transtensional fault would be predicted based on stratal patterns. This low-velocity zone is likely an artifact of the skew ray-path coverage in this region, though it may represent slower lake sediments onlapping the higher velocity sediments to the northeast. The low-velocity zone could potentially be due to a damage zone from the SSAF as well as the proposed STF, though any interpretation is difficult due to the limitations of the ray-path coverage and density in the data gap region (e.g., Fig. 6). Northeast of the damage zone, velocities increase to over 3 km/s, perhaps because of the older formations that exists in this area, which would be more compacted than Lake Cahuilla sands or lake sediments.

The structure creating the observed deformation is not directly imaged or is poorly imaged by MCS data because of gas obscuring the reflectors and shallow water environments. Without direct evidence and imaging of the STF, other hypotheses were investigated to explain the extensional deformation in the strata. One such hypothesis is a southwestward-dipping SSAF with oblique, down-to-the-southwest motion (Kell, 2014). This would not be entirely surprising, because there are many real-world and laboratory examples of extension on faults adjacent to a pull-apart basin. For example, the terminus of the IF in the Cerro Prieto basin appears to be in a transtensional environment (Suarez-Vidal *et al.*, 2008). Another example is observed along the Coronado Bank fault where extension is observed west of San Diego Bay pull-apart basin (Maloney, 2013). In addition, laboratory models (Wu *et al.*, 2009) show spatially sigmoidal patterns of extension on strike-slip faults adjacent to pull-apart basins, such that down-dip direction is orthogonal to the fault and toward the pull-apart basin proper. Extension from the pull-apart basin is consequently imprinted along the adjacent strike-slip faults. This model (a southwest-dipping SSAF), however, would only explain the northeastern dip and extension in the reflectors, not the systematic increase in extension moving north away from the pull-apart basin (e.g., from lines 17 to 19). Furthermore, it is in disagreement with previous interpretations of an eastward dip on the SSAF, based on microseismicity and strain rate from Global Positioning System (GPS) and Interferometric Synthetic Aperture Radar (InSAR; Fialko, 2006; Fuis *et al.*, 2012; Lindsey *et al.*, 2014; Barak *et al.*, 2015).

Dorsey and Langenheim (2015) proposed that the sediment thickening observed in the reflection data in the northern Salton Sea could be due to northeasterly tilting of the Salton block, which simultaneously uplifts the Santa Rosa Mountains. They postulate that an 8°–10° northeasterly rotation and tilting of this block generates accommodation toward the SSAF and would create a fanning dip with depth observed in the reflectors, up to 8°. They include other lines of evidence, such as results from gravity models and the proposed asymmetric topography across the Santa Rosa Mountains. The reflection data presented in this study could be consistent with the predictions made by the Dorsey and Langenheim conceptual model, with a few caveats and differences required to honor the observed stratigraphic relationships. First, according

to their model, accommodation for sediment accumulation would be destroyed to the west and created to the east of the fulcrum for Salton block rotation. Therefore, the fulcrum of tilting must be at or very near the western Salton Sea shoreline. Otherwise, if it was farther west as postulated by Dorsey and Langenheim (2015), attendant erosion in the southwest would cause sediment progradation to the northeast, infilling the newly created accommodation. This is not observed in the seismic-reflection data (Figs. 3 and 7). Second, the newly acquired reflection data require that there be a fault structure west of the SSAF controlling the northeast-dipping diverging reflectors. Reasons for this are threefold: (1) the sediments onshore are old lake deposits of late Pleistocene age (Borrego Fm) and are highly deformed, faulted and folded, and steeply dipping to the southwest. In contrast, the stratigraphy in the sea is undeformed and gently dipping to the northeast ($\sim$ <2°). A breakaway zone must exist between the older, highly deformed onshore sediments and younger, undeformed and gently dipping offshore sediments, which extend down to at least 2 km in thickness (Fig. 3). (2) A scarp is observed in the bathymetry and there is a marked change in the gradient (Fig. 13). Such a marked change, and observed scarp, is best explained by the presence of a fault west of the Salton Sea shoreline. (3) The divergence and tilting increase to the north in the Salton Sea, less in line 17 and increasing systematically towards lines 7 and 19 away from the highest topography onshore. If loading from convergence across the southeast-dipping SSAF caused the tilting (Fig. 14) then a correlation should exist between the highest topography on the hanging wall and the greatest subsidence in the footwall (Christie-Blick and Driscoll, 1995). This relationship is not observed (Fig. 1). In fact the gravity data presented by Dorsey and Langenheim (2015; their fig. 2) are consistent with an increase in subsidence toward the north in the Salton Sea, as observed in the seismic-reflection data. Finally, it is important to note that the observed dips of the reflectors in lines 19, 7, and 17 is at most 2°, less than that reported in Dorsey and Langenheim (2015).

As mentioned above, these new seismic data are consistent with the Dorsey and Langenheim (2015) model; magnetic and gravity data place important constraints on basement architecture, and seismic-reflection data provide additional constraints on the sediment structure. Nevertheless, the alternative model presented here (i.e., the STF) could also explain the seismic observations, without requiring regional tilting of the Salton block (Fig. 14). Additional research is required to test between these two alternative models.

Deformation on the STF is presumed to be long-lived due to the persistence of deformation observed in the MCS profiles, down to at least 1.8 s ($\sim$2 km) TWTT. Surficial deformation observed on both the shallow 2010 and deeper 2011 MCS records recent activity on the structure responsible for this geometry. Despite these observations, there is an absence of microseismicity in the regions surrounding this structure. Seismicity is observed along the SSAF (Lin *et al.*, 2007) along a presumed-dipping structure; however, there is no seismicity on the proposed location of the STF. This lack of historical

seismicity suggests that the STF is not creeping (Sanders and Kanamori, 1984; Rubin *et al.*, 1999) or that the strain has been distributed on other structures in the region.

To the north, there is a visible fault scarp offshore just adjacent to the shoreline (Fig. 13), but it is difficult to discern any tectonic signal in the onshore lidar data north of the sea due to anthropogenic activity; therefore, it is not clear if and where the STF continues onshore north of the Salton Sea. InSAR data (Tong *et al.*, 2013) show a faint trend of uplift, or motion toward the satellite, continuing onshore of the proposed STF location. The strike in this trend is similar to the expected strike of the STF; however, it is noted in Tong *et al.*, (2013) that this could be due to agricultural or anthropogenic activity. Janecke (2013) also proposes the existence of a structure west of the SSAF, the East Shoreline fault, which is predominantly onshore; however, our proposed fault (STF) is projected to be in the Salton Sea, west of the shoreline. Although the SSAF is interpreted to be transpressional near Durmid Hill, there are examples in other regions around the world where transtensional and transpressional or strike-slip faults have been found to be parallel to each other, or in close proximity to each other (Wilcox *et al.*, 1973; Mann *et al.*, 1983; Chanes-Martínez *et al.*, 2014; Maloney *et al.*, 2016).

Figure 14 is a schematic of the preferred hypothesis including the existence of the STF. The first panel describes the observations for the region, including geomorphic features as well as MCS data and geologic observations from Babcock (1974). The second panel describes the preferred hypothesis for the region; it shows the STF just southwest of the Salton Sea shoreline with folded strata between the STF and SSAF. The third panel is a subset of the second panel, showing in detail the MCS, refraction and geologic observations. The seismic low-velocity zone may be caused by shallow lake sediments onlapping higher velocity older sediments to the northeast (or potentially a highly deformed material between the STF and SSAF). The final panel is modified from Dorsey and Langenheim (2015) showing the rotation of the Salton block. The rotation is driven by extensional unloading along the southwest-dipping Santa Rosa fault and compressional loading along the SSAF.

It is important to consider the implications of a previously unmapped transtensional structure in this location. Currently, hazard in a given area quantified by ground-motion prediction equations (GMPEs) is determined by a variety of factors, including the earthquake magnitude, dip of a fault, as well as style-of-faulting (Bommer *et al.*, 2003; Campbell and Bozorgnia, 2012). The presence of a transtensional structure would affect the dip and style-of-faulting considered in these equations and thus the predictions from GMPE's for the region.

The STF could also significantly alter predictions from physics-based ground-motion prediction methods. The STF could trigger or be triggered by rupture on the SSAF, increasing the magnitude or complicating rupture geometry. Additionally, radiation patterns of body and surface waves are a direct consequence of the strike, dip, and rake of the fault responsible for an earthquake (Aki and Richards, 1980). Trig-

gering of the STF would alter the expected radiation pattern caused by an earthquake, in turn affecting seismic wave propagation. This could potentially cause even more amplification in the sedimentary basins of southern California than was predicted by TeraShake (Olsen *et al.*, 2006). The San Bernardino, Chino, San Gabriel, and Los Angeles basins act as a waveguide into Los Angeles, further exciting waves that are trapped within these basins. Furthermore, 3D models of rupture on thrust, normal, and strike-slip faults (Oglesby *et al.*, 2000; Oglesby and Day, 2001; Duan, 2010) show that the hanging wall of faults experience larger final displacements, as well as peak ground velocities (PGVs), regardless of the style-of-faulting. When applied to the proposed geometry for the STF, this could suggest that PGVs and final displacements would be larger to the southwest of the fault. Most of these rupture models, however, focus on thrust and strike-slip events and few on oblique events.

Conclusions

The marine active-source seismic-reflection and refraction data presented here provide strong evidence for a transtensional structure, the STF, near the eastern shoreline of the Salton Sea. Additionally, the fault scarp observed in bathymetric data and the strata and folding observed in the lidar data suggest that the STF is within the Salton Sea and west of the SSAF. This previously unidentified fault represents a new hazard to the region and holds significant implications for fault models such as the Southern California Earthquake Center Community Fault Model (SCEC CFM) and, consequently, models of ground-motion prediction and SSAF rupture scenarios. Future ground-motion simulation models, as well as GPS studies, should consider this possibility. More research is required to test this new model, based on the newly acquired seismic reflection.

Data and Resources

The multichannel seismic data used in this study were acquired as part of a National Science Foundation grant. The data are archived at the Lamont Doherty Earth Observatory (http://www.ldeo.columbia.edu/research/databases-repositories), and University of Texas Institute of Geophysics (http://www-udc.ig.utexas.edu/sdc/). The Ocean Bottom Seismometer (OBS) data were acquired as a part of this project, and are available on the Incorporated Research Institutions for Seismology (IRIS) website. Finally, light detection and ranging (lidar) data were acquired for this investigation, and are archived on OpenTopography (opentopography.org). This study did not visit these sites to download the data, as the investigation was performed on collected data and later provided to these sites.

Acknowledgments

References

Aki, K., and P. G. Richards (1980). *Qualitative Seismology*, University Press Science Books, Sausalito, California.

Babcock, E. A. (1974). Geology of the northeast margin of the Salton trough, Salton Sea, California, *Geol. Soc. Am. Bull.* **85,** no. 3, 321–332, doi: 10.1130/0016-7606(1974)85<321:GOTNMO>2.0.CO;2.

Barak, S., S. L. Klemperer, and J. F. Lawrence (2015). San Andreas Fault dip, Peninsular Ranges mafic lower crust and partial melt in the Salton Trough, Southern California, from ambient-noise tomography, *Geochem. Geophys. Geosys.* **16,** no. 11, 3946–3972, doi: 10.1002/2015GC005970.

Bennett, R. A., W. Rodi, and R. E. Reilinger (1996). Global positioning system constraints on fault slip rates in southern California and northern Baja, *Mexico J. Geophys. Res.* **101,** no. B10, 21,943–21,960.

Bommer, J. J., J. Douglas, and F. O. Strasser (2003). Style-of-faulting in ground-motion prediction equations, *Bull. Earthq. Eng.* **1,** no. 2, 171–203, doi: 10.1023/A:1026323123154.

Brothers, D., D. Kilb, K. Luttrell, N. Driscoll, and G. Kent (2011). Loading of the San Andreas fault by flood-induced rupture of faults beneath the Salton Sea, *Nature Geosci.* **4,** no. 7, 486–492, doi: 10.1038/ngeo1184.

Brothers, D. S., N. W. Driscoll, G. M. Kent, A. J. Harding, J. M. Babcock, and R. L. Baskin (2009). Tectonic evolution of the Salton Sea inferred from seismic reflection data, *Nature Geosci.* **2,** no. 8, 581–584, doi: 10.1038/NGEO590.

Bürgmann, R. (1991). Transpression aong the southern San Andreas fault, Durmid Hill, California, *Tectonics* **10,** no. 6, 1152–1163, doi: 10.1029/91TC01443.

Campbell, K. W., and Y. Bozorgnia (2012). NGA ground motion model for the geometric mean horizontal component of PGA, PGV, PGD, and 5% damped linear elastic response spectra for periods ranging from 0.01 to 10 s, *Earthq. Spectra* **24,** no. 1, 139–171, doi: 10.1193/1.2857546.

Chanes-Martínez, J. J., M. González-Escobar, F. Suárez-Vidal, and C. G. Gallardo-Mata (2014). Structural geometry of a sector of the Colorado River delta, Baja California, Mexico, based on seismic reflections, *Pure Appl. Geophys.* **171,** no. 7, 1107–1127.

Christie-Blick, N., and N. W. Driscoll (1995). Sequence stratigraphy, *Ann. Rev. Earth Planet. Sci.* **23,** 451–478, doi: 10.1146/annurev.ea.23.050195.002315.

Deal, M. M., and G. Nolet (1996). Nullspace shuttles, *Geophys. J. Int.* **124,** no. 2, 372–380, doi: 10.1111/j.1365-246X.1996.tb07027.x.

Dingler, J., G. Kent, N. Driscoll, J. Babcock, A. Harding, G. Seitz, B. Karlin, and C. Goldman (2009). A high-resolution seismic CHIRP investigation of active normal faulting across Lake Tahoe basin, California-Nevada, *Geol. Soc. Am. Bull.* **121,** nos. 7/8, 1089–1107.

Dorsey, R. J., and V. E. Langenheim (2015). Crustal-scale tilting of the central Salton block, southern California, *Geosphere* **11,** no. 5, 1–19, doi: 10.1130/GES01167.1.

Driscoll, N. W., and G. D. Karner (1998). Lower crustal extension across the Northern Carnarvon basin, Australia: Evidence for an eastward dipping detachment, *J. Geophys. Res.* **103,** no. B3, 4975–4991.

Driscoll, N. W., J. R. Hogg, N. Christie-Blick, and G. D. Karner (1995). Extensional tectonics in the Jeanne d'Arc basin, offshore Newfoundland: Implications for the timing of break-up between Grand Banks and Iberia, *Geol. Soc. Lond. Spec. Publ.* **90,** no. 1, 1–28.

Duan, B. (2010). Role of initial stress rotations in rupture dynamics and ground motion: A case study with implications for the Wenchuan earthquake, *J. Geophys. Res.* **115,** no. B5, B05301, doi: 10.1029/2009JB006750.

Eisses, A. K., A. Kell, G. M. Kent, N. W. Driscoll, R. L. Baskin, K. D. Smith, R. E. Karlin, J. N. Louie, and S. K. Pullammanappallil (2015). New constraints on fault architecture, slip rates, and strain partitioning beneath Pyramid Lake, *Nevada Geosphere* **11,** no. 3, 683–704, doi: 10.1130/GES00821.1.

Farr, T. G., P. A. Rosen, E. Caro, R. Crippen, R. Duren, S. Hensley, M. Kobrick, M. Paller, E. Rodriguez, L. Roth, *et al.* (2007). The shuttle radar topography mission, *Rev. Geophys.* **45,** no. 2, doi: 10.1029/2005RG000183.

Fay, N. P., and E. D. Humphreys (2005). Fault slip rates, effects of elastic heterogeneity on geodetic data, and the strength of the lower crust in the Salton trough region, southern California, *J. Geophys. Res.* **110,** no. B9, 2156–2202, doi: 10.1029/2004JB003548.

Fialko, Y. (2006). Interseismic strain accumulation and the earthquake potential on the southern San Andreas fault system, *Nature* **441,** no. 7096, 968–971, doi: 10.1038/nature04797.

Fuis, G. S., D. S. Scheirer, V. E. Langenheim, and M. D. Kohler (2012). A new perspective on the geometry of the San Andreas fault in southern California and its relationship to lithospheric structure, *Bull. Seismol. Soc. Am.* **102,** no. 1, 236–251, doi: 10.1785/0120110041.

Hartzell, S. H., and T. H. Heaton (1983). Inversion of strong ground motion and teleseismic waveform data for the fault rupture history of the 1979 Imperial-Valley, California, earthquake, *Bull. Seismol. Soc. Am.* **73,** no. 6, 1553–1583.

Janecke, S. U. (2013). Testing a step-over model of the southern San Andreas fault at Durmid Hill, *SCEC Final Report*, 1–9.

Kell, A. M. (2014). The application of active-source seismic imaging techniques to transtensional problems in the Walker Land and Salton trough, *Ph.D. Thesis*, University of Nevada, Reno.

Kell, A. M., V. J. Sahakian, A. J. Harding, G. M. Kent, and N. W. Driscoll (2012). Shallow sediment and upper crustal structure beneath the Salton Sea as imaged by active source marine seismic refraction in conjunction with the Salton Seismic Imaging Project, presented at *2012 Fall Meeting*, AGU, San Francisco, California, 3–7 December, Abstract T51B-2578.

Kent, G. M., J. M. Babcock, N. W. Driscoll, A. J. Harding, J. A. Dingler, G. G. Seitz, J. V. Gardner, L. A. Mayer, C. R. Goldman, A. C. Heyvaert, *et al.* (2005). 60 k.y. record of extension across the western boundary of the Basin and Range province: estimate of slip rates from offset shoreline terraces and a catastrophic slide beneath Lake Tahoe, *Geology* **33,** 365–368.

Lin, G., P. M. Shearer, and E. Hauksson (2007). Applying a three-dimensional velocity model, waveform cross correlation, and cluster analysis to locate southern California seismicity from 1981 to 2005, *J. Geophys. Res.* **112,** no. B12, doi: 10.1029/2007JB004986.

Lindsey, E. O., Y. Fialko, Y. Bock, D. T. Sandwell, and R. Bilham (2014). Localized and distributed creep along the southern San Andreas fault, *J. Geophys. Res.* **119,** no. 10, 7909–7922, doi: 10.1002/2014JB011275.

Lundgren, P., E. A. Hetland, Z. Liu, and E. J. Fielding (2009). Southern San Andreas-San Jacinto fault system slip rates estimated from earthquake cycle models constrained by GPS and interferometric synthetic aperture radar observations, *J. Geophys. Res.* **114,** no. B2, 2156–2202, doi: 10.1029/2008JB005996.

Lynch, D. K., and K. W. Hudnut (2008). The Wister mud pot lineament: Southeastward extension or abandoned strand of the San Andreas fault? *Bull. Seismol. Soc. Am.* **98,** no. 4, 1720–1729, doi: 10.1785/0120070252.

Maloney, J. M. (2013). Fault segments and step-overs: Implications for geohazards and biohabitats, *Ph.D. Thesis*, University of California, San Diego.

Maloney, J. M., N. Driscoll, G. Kent, S. Duke, T. Freeman, and J. Bormann (2016). Segmentation and step-overs along strike-slip fault systems in the inner California borderlands: Implications for fault architecture and basin formation, in *Applied Geology in California, Environmental*

Engineering Geologists, R. Anderson and H. Ferriz (Editors), special publication 26, Chapter 36, 655–677.

Maloney, J. M., P. J. Noble, N. W. Driscoll, G. M. Kent, S. B. Smith, G. C. Schmauder, J. Babcock, R. Baskin, R. Karlin, A. M. Kell, *et al.* (2013). Paleoseismic history of the Fallen Leaf segment of the West Tahoe-Dollar Point fault reconstructed from slide deposits in the Lake Tahoe basin, California-Nevada, *Geosphere* **9,** no. 4, 1065–1090.

Mann, P., M. R. Hempton, D. C. Bradley, and K. Burke (1983). Development of pull-apart basins, *J. Geol.* **91,** no. 5, 529–554, doi: 10.1086/628803.

Oglesby, D. D., and S. M. Day (2001). Fault geometry and the dynamics of the 1999 Chi-Chi (Taiwan) earthquake, *Bull. Seismol. Soc. Am.* **91,** no. 5, 1099–1111, doi: 10.1785/0120000714.

Oglesby, D. D., R. J. Archuleta, and S. B. Nielsen (2000). The three-dimensional dynamics of dipping faults, *Bull. Seismol. Soc. Am.* **90,** no. 3, 616–628, doi: 10.1785/0119990113.

Olsen, K. B., S. M. Day, J. B. Minster, Y. Cui, A. Chourasia, R. Moore, P. Maechling, and T. Jordan (2006). Strong shaking in Los Angeles expected from southern San Andreas earthquake, *Geophys. Res. Lett.* **33,** no. 7, L07305, doi: 10.1029/2005GL025472.

Philibosian, B., T. Fumal, and R. Weldon (2011). San Andreas fault earthquake chronology and Lake Cahuilla history at Coachella, California, *Bull. Seismol. Soc. Am.* **101,** no. 1, 13–38, doi: 10.1785/0120100050.

Rose, E. J., G. S. Fuis, J. M. Stock, J. A. Hole, A. M. Kell, G. M. Kent, N. W. Driscoll, A. M. Reusch, L. Han, R. R. Sickler, *et al.* (2013). Borehole-explosion and air-gun data acquired in the 2011 Salton Seismic Imaging Project (SSIP), southern California: Description of the survey, *U.S. Geol. Surv. Open-File Rept. 2013–1172*, doi: 10.3133/ofr20131172.

Rubin, A. M., D. Gillard, and J. L. Got (1999). Streaks of microearthquakes along creeping faults, *Nature* **400,** no. 6745, 635–641, doi: 10.1038/23196.

Sahakian, V. J. (2015). Architecture and segmentation of strike-slip faults in southern California, *Ph.D. Thesis*, University of California, San Diego, ISBN: 9781339144740.

Sanders, C. O., and H. Kanamori (1984). A seismotectonic analysis of the Anza seismic gap, San Jacinto fault zone, southern California, *J. Geophys. Res.* **89,** no. B7, 5873–5890, doi: 10.1029/JB089iB07p05873.

Suarez-Vidal, F., R. Mendoza-Borunda, L. M. Nafarrete-Zamarripa, J. Ramirez, and E. Glowacka (2008). Shape and dimensions of the Cerro Prieto pull-apart basin, Mexicali, Baja California, Mexico, based on the regional seismic record and surface structures, *Int. Geo. Rev.* **50,** no. 7, 636–649, doi: 10.2747/0020-6814.50.7.636.

Thomas, A. P., and T. K. Rockwell (1996). A 300- to 550-year history of slip on the Imperial fault near the US-Mexico border: Missing slip at the Imperial fault bottleneck, *J. Geophys. Res.* **101,** no. B3, 5987–5997, doi: 10.1029/95JB01547.

Tong, X., D. T. Sandwell, and B. Smith-Konter (2013). High-resolution interseismic velocity data along the San Andreas fault from GPS and InSAR, *J. Geophys. Res.* **118,** no. 1, 369–389, doi: 10.1029/2012JB009442.

Van Avendonk, H. J. A., D. J. Shillington, W. S. Holbrook, and M. J. Hornbach (2004). Inferring crustal structure in the Aleutian island arc from a sparse wide-angle seismic data set, *Geochem. Geophys. Geosys.* **5,** no. 8, Q08008, doi: 10.1029/2003GC000664.

Waters, M. R. (1983). Late Holocene lacustrine chronology and archaeology of ancient Lake Cahuilla, California, *Quaternary Res.* **19,** no. 3, 373–387, doi: 10.1016/0033-5894(83)90042-X.

Wilcox, R. E., T. T. Harding, and D. R. Seely (1973). Basic wrench tectonics, *AAPG Bulletin* **57,** no. 1, 74–96.

Wu, J. E., K. McClay, P. Whitehouse, and T. Dooley (2009). 4D analogue modelling of transtensional pull-apart basins, *Mar. Petrol. Geol.* **26,** no. 8, 1608–1623.

Scripps Institution of Oceanography
University of California, San Diego
9500 Gilman Drive, Mail Code 0220
La Jolla, California 92093-0225
        (V.S., N.D.)

Nevada Seismological Laboratory
University of Nevada, Reno
1664 North Virginia Street
Reno, Nevada 89557-0174
        (A.K., G.K.)

Scripps Institution of Oceanography
University of California, San Diego
9500 Gilman Drive, Mail Code 0225
La Jolla, California 92093-0225
        (A.H.)